Electronic Supplementary Material (ESI) for Materials Chemistry Frontiers.

Supporting Information for

Bright electrochemiluminescence films of efficient aggregation-induced emission luminogens for sensitive detection of dopamine

Zihua Li,[a] Wei Qin,*[,a] Jialong Wu,[a] Zhiyong Yang,[b] Zhenguo Chi,[b] Guodong Liang*[,a]

[a]*PCFM lab, School of Materials Science and Engineering, Sun Yat-sen University, Guangzhou, 510275, China.*

[b]*PCFM lab, School of Chemistry, Sun Yat-sen University, Guangzhou, 510275, China.*

* Corresponding author: Tel: +86-20-84004033; Fax: +86-20-84004033

E-mail address: qinw9@mail.sysu.edu.cn, lgdong@mail.sysu.edu.cn

Table of Contents

1. Experimental section

1.1 Materials

4,7-dibromo-2,1,3-benzothiadiazole, phenylboronic acid, 4-(diphenylamino) phenylboronic acid, (4-(naphthalen-1-yl(phenyl)-amino)phenyl)boronic acid, tetrakis(triphenylphosphine)palladium, potassium carbonate, tetrabutylammonium hexafluorophosphate ($TBAPF_6$), Benzoyl peroxide (BPO), ascorbic acid (AA), uric acid (UA), tetrahydrofuran (THF), dichloromethane (DCM), cyclohexane (CH), toluene (Tol), *N*, *N*-Dimethylformamide (DMF), and acetonitrile (CH_3CN) were purchased from Energy Chemical or Soochiral Chemical Science & Technology in China. Dopamine hydrochloride (DA), Tri-*n*-propanamine (TPrA), 2-mercapoethanol (*β*ME) were obtained from Macklin (China). All regents or chemicals were used as received without any further purification.

1.2 Apparatus and characterization

All organic compounds were characterized by nuclear magnetic resonance (NMR) and high-resolution mass spectra (HRMS). The ^1H NMR spectra were measured on a Bruker AV 400 spectrometer in $CDCl_3$ with tetramethylsilane (TMS) as an internal reference. The high-resolution mass spectra (HRMS) were recorded using a mass spectrometer (LTQ XL, ThermoFisher, America) operating in matrix-assisted laser desorption ionization time-of-flight (MALDI-TOF) mode. Optimized geometries and molecular orbitals of HOMO and LUMO levels of **BTD-Ph**, **BTD-TPA**, and **BTD-NPA** were calculated using a density functional theory (DFT) method (B3LYP/6-31+(d) of the optimized structures; Gaussian 09). UV-vis absorbance spectra were

recorded with a SOPTOP 752 spectrometer. PL spectra were measured on a GANGDONG F-380 spectrofluorometer. Quantum yields of **BTD-Ph**, **BTD-TPA**, and **BTD-NPA** in solid powders were recorded by using an Edinburgh Instruments spectrometer (FLSP920) with a calibrated integrating sphere. The morphologies of **BTD-TPA** films were characterized by scanning electron microscopy (SEM, Quanta 400, FEI Company). The X-ray diffraction (XRD) pattern was recorded on an X-ray diffractometer (XRD, D8 Advance, Bruker) with Cu Ka radiation. All the digital photos were recorded with an Apple iPhone X.

2. Synthetic protocols of the compounds

2.1 Synthesis of BTD-Ph

A mixture of 4,7-dibromo-2,1,3-benzothiadiazole (147 mg, 0.5 mmol), phenylboronic acid (183 mg, 1.5 mmol), $Pd(PPh_3)_4$ (50 mg, 0.04 mmol), K_2CO_3 (690 mg, 5 mmol), THF (40 mL) and water (8 mL) was heated to 60 °C for 24 h under nitrogen and stirring. The mixture was cooled to room temperature. After vacuum concentration of the mixture, dichloromethane (150 mL) and water (50 mL) were added. An organic layer was separated and washed with water (150 mL) three times, dried over anhydrous Na_2SO_4 and evaporated to dryness under reduced pressure. The crude product was purified by column chromatography on silica gel using hexane/dichloromethane as eluent. ^{1}H NMR (400 MHz, $CDCl_3$) δ (ppm): 7.47 (t, 2H, Ar H), 7.56 (t, 4H, Ar H), 7.80 (s, 2H, Ar H), 7.97 (d, 4H, Ar H); HRMS (MALDI-TOF) *m*/*z*: [M^+] calcd for $C_{18}H_{12}N_2S$, 289.0755; found, 288.0793.

2.2 Synthesis of BTD-TPA

A mixture of 4,7-dibromo-2,1,3-benzothiadiazole (147 mg, 0.5 mmol), 4-(diphenylamino)phenylboronic acid (434 mg, 1.5 mmol), $Pd(PPh_3)_4$ (50 mg, 0.04 mmol), K_2CO_3 (690 mg, 5 mmol), THF (40 mL) and water (8 mL) was heated to 60 °C for 24 h under nitrogen and stirring. The mixture was cooled to room temperature. After vacuum concentration of the mixture, dichloromethane (150 mL) and water (50 mL) were added. An organic layer was separated and washed with water (150 mL) three times, dried over anhydrous Na_2SO_4 and evaporated to dryness under reduced pressure. The crude product was purified by column chromatography on silica gel using hexane/dichloromethane as eluent. ^{1}H NMR (400 MHz, $CDCl_3$) δ (ppm): 7.06 (t, 2H, Ar H), 7.20 (t, 12H, Ar H), 7.29 (t, 8H, Ar H), 7.74 (t, 2H, Ar H), 7.88 (d, 4H, Ar H); ^{13}C NMR (125 MHz, $CDCl_3$) δ (ppm): 123.3, 124.9, 127.4, 129.4, 129.9, 131.0, 132.2, 147.5, 148.0, 154.2; HRMS (MALDI-TOF) *m/z*: [M^+] calcd for $C_{42}H_{30}N_4S$, 622.2191; found, 622.1989.

2.3 Synthesis of BTD-NPA

A mixture of 4,7-dibromo-2,1,3-benzothiadiazole (147 mg, 0.5 mmol), (4-(naphthalen-1-yl(phenyl)-amino)phenyl)boronic acid (509 mg, 1.5 mmol), $Pd(PPh_3)_4$ (50 mg, 0.04 mmol), K_2CO_3 (690 mg, 5 mmol), THF (40 mL) and water (8 mL) was heated to 60 °C for 24 h under nitrogen and stirring. The mixture was cooled to room temperature. After vacuum concentration of the mixture, dichloromethane (150 mL) and water (50 mL) were added. An organic layer was separated and washed with water (150 mL) three times, dried over anhydrous Na_2SO_4 and evaporated to dryness under reduced pressure.

The crude product was purified by column chromatography on silica gel using hexane/dichloromethane as eluent. ^{1}H NMR (400 MHz, $CDCl_3$) δ (ppm): 6.99 (t, 2H, Ar H), 7.10-7.24 (m, 12H, Ar H), 7.36-7.54 (m, 8H, Ar H), 7.69 (s, 2H, Ar H), 7.82 (t, 6H, Ar H), 7.90 (d, 2H, Ar H) , 8.00 (d, 2H, Ar H); ^{13}C NMR (125 MHz, $CDCl_3$) δ (ppm): 120.8, 122.4, 122.6, 124.2, 126.2, 126.4, 126.6, 126.8, 127.3, 127.6, 128.4, 129.2, 129.8, 130.1, 131.4, 132.1, 135.3, 143.1, 147.9, 148.5, 154.2; HRMS (MALDI-TOF) *m*/*z*: [M^+] calcd for $C_{50}H_{34}N_4S$, 722.2504; found, 722.2363.

3. Supplementary figures

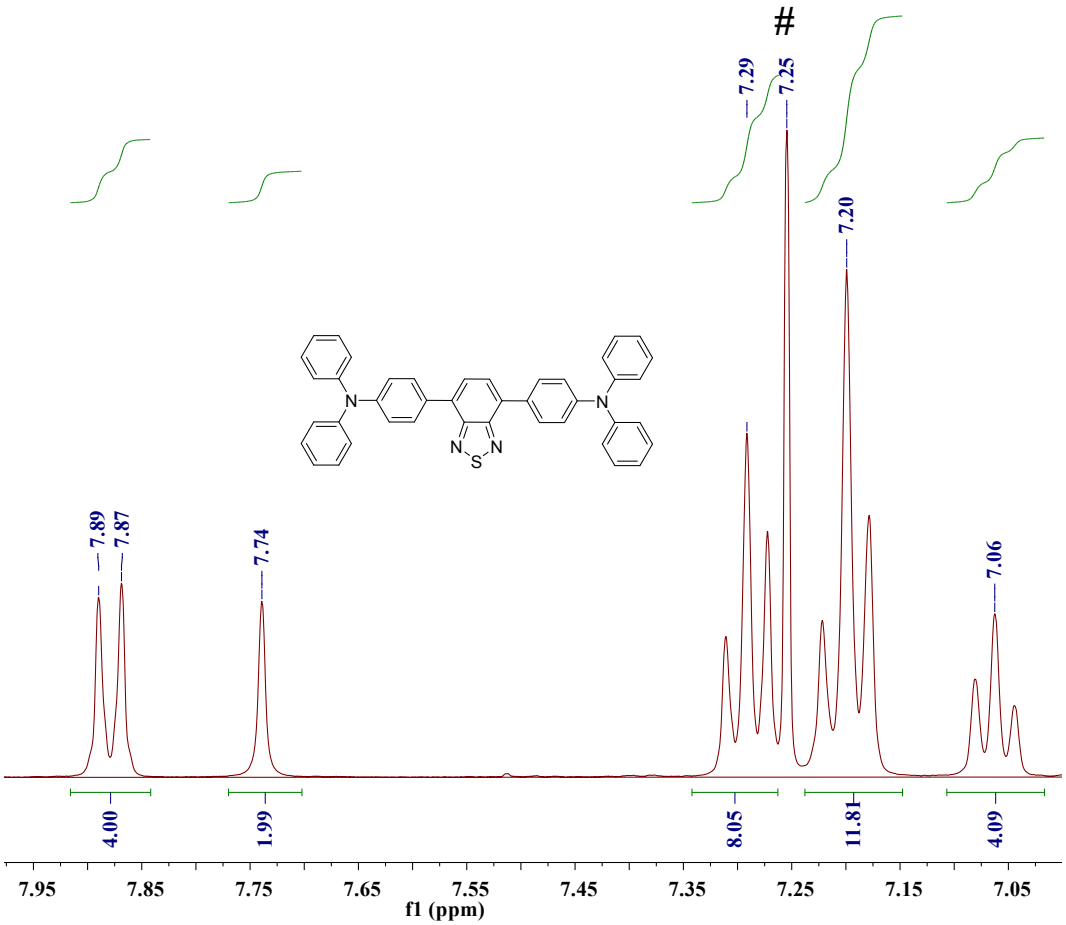

Fig. S1 ^{1}H NMR spectrum of **BTD-TPA** in $CDCl_3$ (# $CDCl_3$).

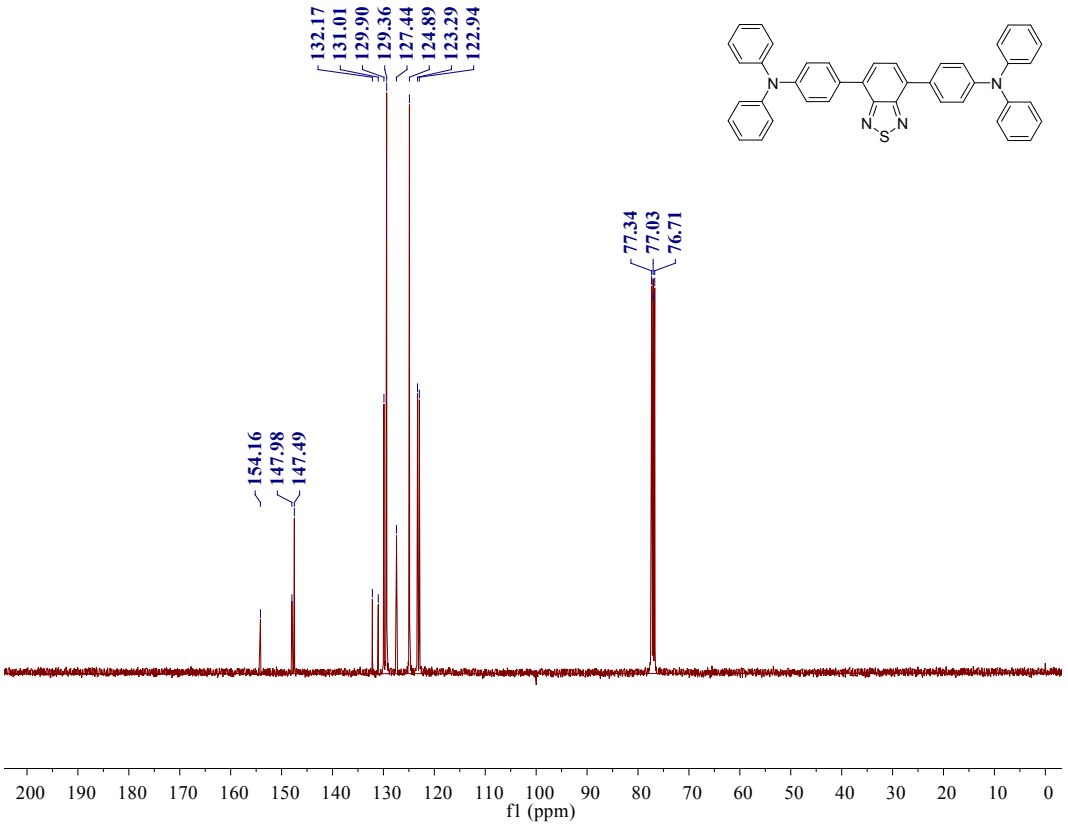

Fig. S2 ^{13}C NMR spectrum of **BTD-TPA** in $CDCl_3$.

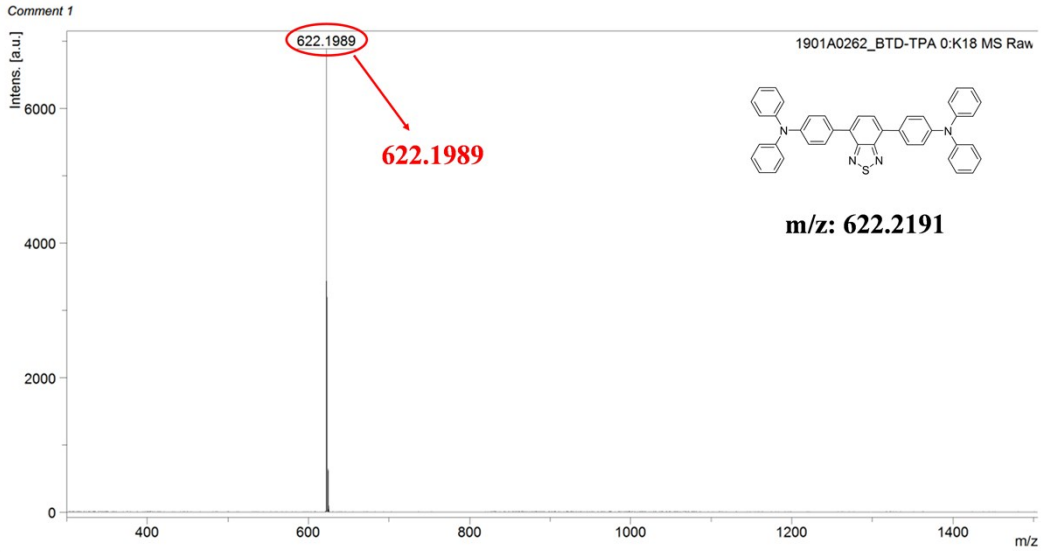

Fig. S3 HRMS spectrum of **BTD-TPA**.

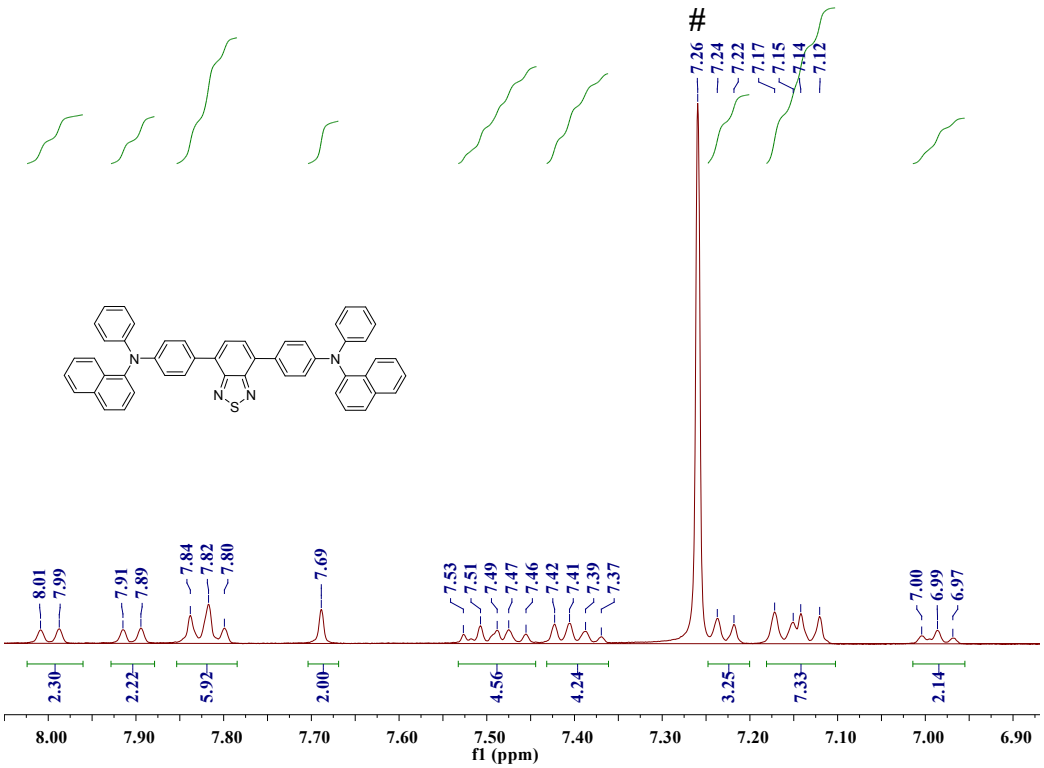

Fig. S4 ^{1}H NMR spectrum of **BTD-NPA** in $CDCl_3$ (# $CDCl_3$).

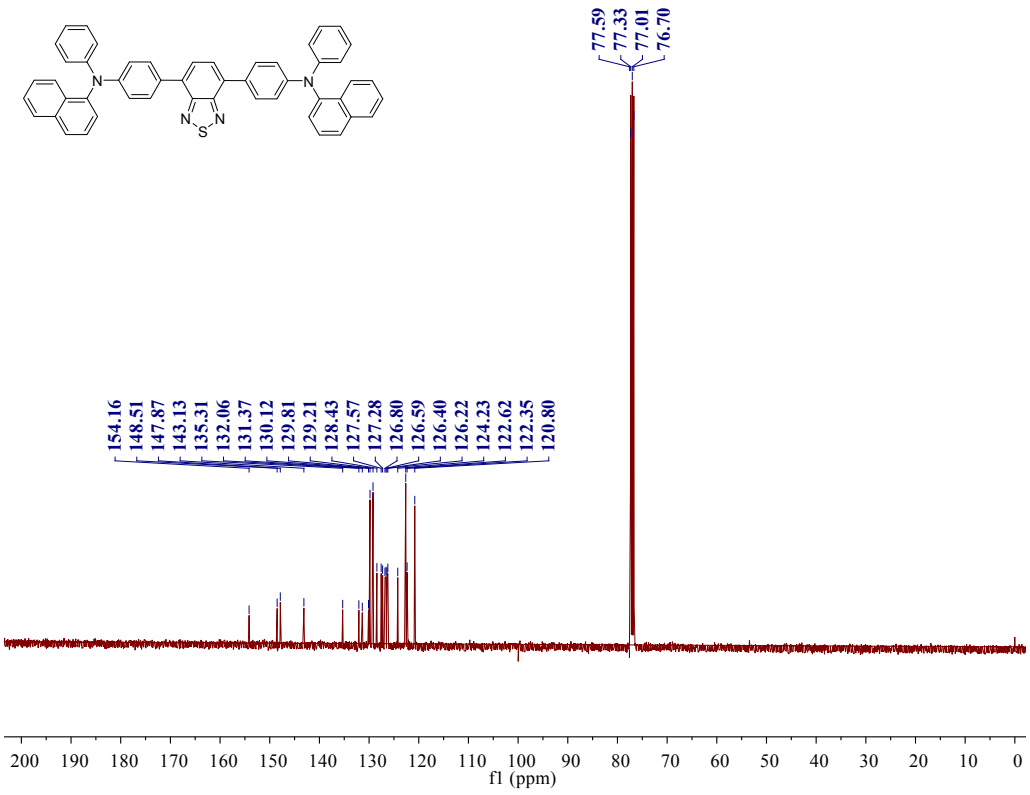

Fig. S5 ^{13}C NMR spectrum of **BTD-NPA** in $CDCl_3$.

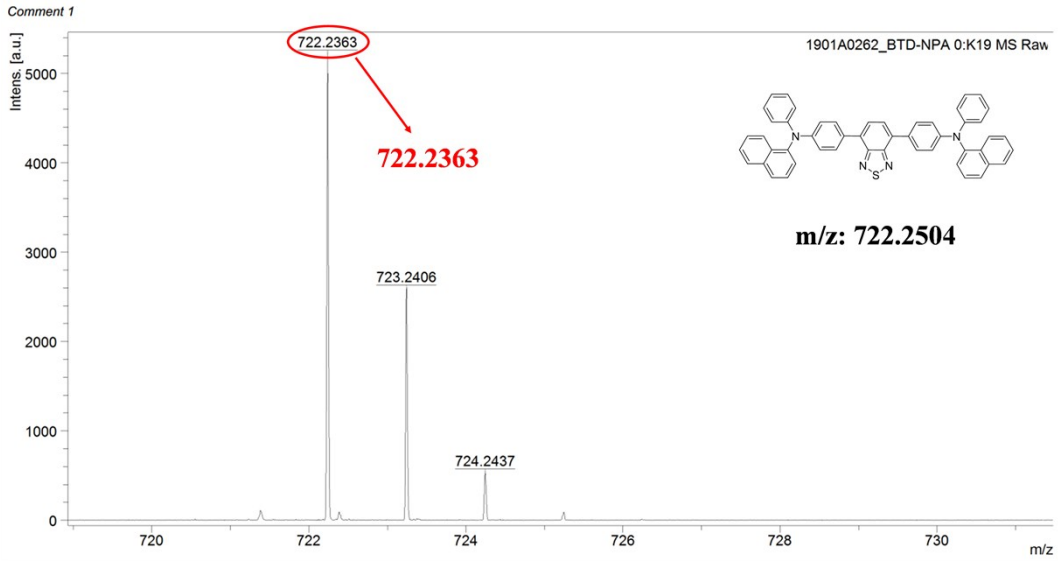

Fig. S6 HRMS spectrum of **BTD-NPA**.

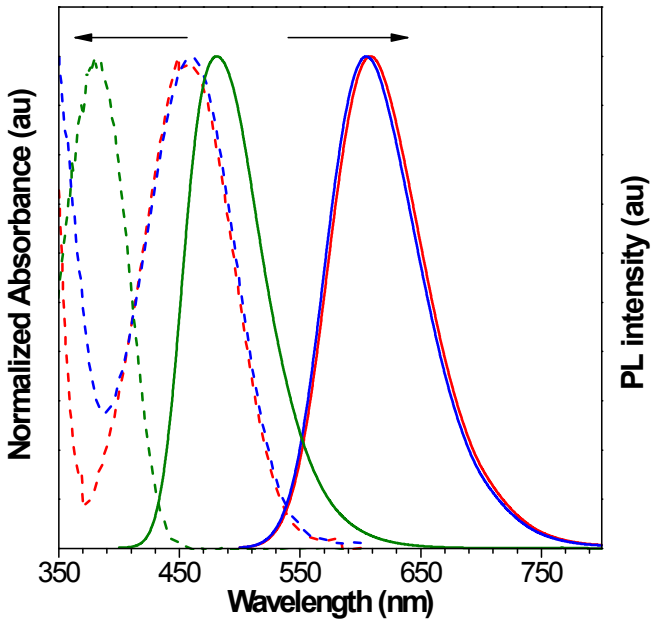

Fig. S7 Normalized UV-vis (dash) and PL emission (solid) spectra of **BTD-Ph** (green), **BTD-TPA** (red), and **BTD-NPA** (blue) in THF solution. Concentration: 10 μM.

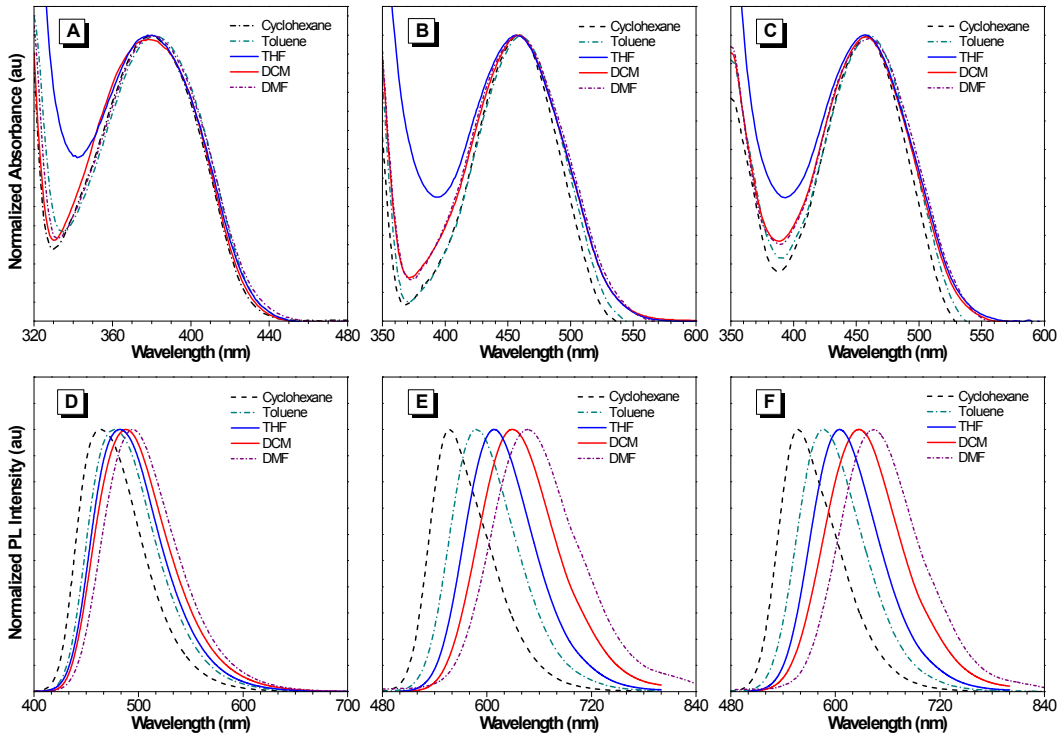

Fig. S8 Normalized absorption and PL emission spectra of (A and D) **BTD-Ph**, (B and E) **BTD-TPA**, and (C and F) **BTD-NPA** in solvents with different polarities.

Table S1. The absorption and emission wavelength of **BTD-Ph**, **BTD-TPA**, and **BTD-NPA** in different solvents.

Compound	λ_{ab} [nm]					λ_{PL} [nm]				
	CH	Tol	THF	DCM	DMF	CH	Tol	THF	DCM	DMF
BTD-Ph	380	382	380	380	381	464	476	481	488	495
BTD-TPA	459	460	458	459	459	557	588	609	630	646
BTD-NPA	459	461	458	459	461	557	586	605	627	640

The UV spectra of the same molecule in different solvents are peaked at similar wavelengths (Fig. S8 and Table S1). While the solvent polarity is increased from cyclohexane (CH) to *N,N*-dimethylformamide (DMF), the emission peaks of the studied molecules are red-shifted.

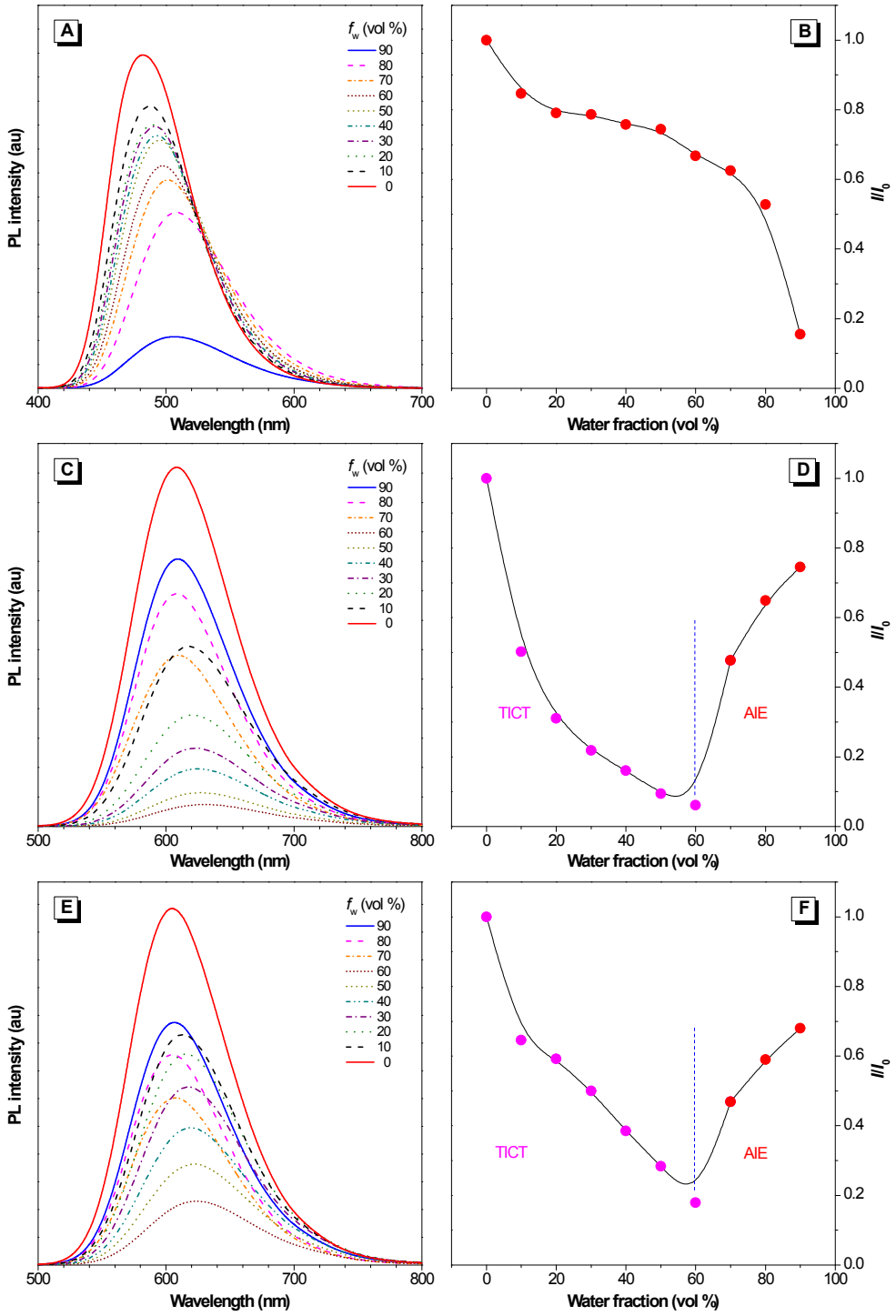

Fig. S9 PL spectra of (A) **BTD-Ph**, (C) **BTD-TPA**, and (E) **BTD-NPA**. Plot of relative PL intensity (I/I_0) versus water fractions (f_w) of (B) **BTD-Ph**, (D) **BTD-TPA**, and (F) **BTD-NPA** in THF/water mixtures. I_0: emission intensity in pure THF. Compounds concentration: 10 μM; λ_{ex} = 380 nm, 460 nm and 461 nm for **BTD-Ph**, **BTD-TPA**, and **BTD-NPA**, respectively.

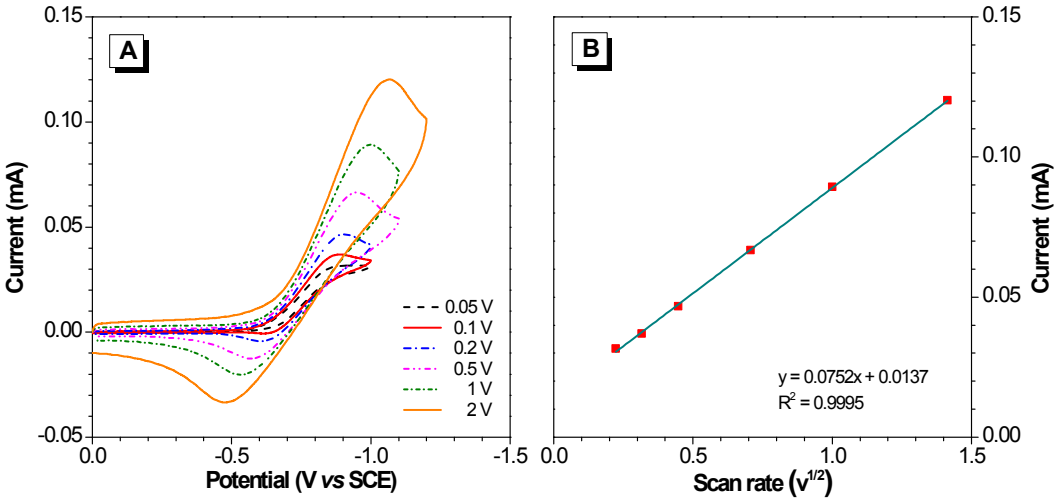

Fig. S10 Cyclic voltammograms of 1 mM **BTD-Ph** in DCM with 0.1 M $TBAPF_6$ at various scan rates; (A) reduction voltammogram of **BTD-Ph**, and (B) reduction peak current *versus* $v^{1/2}$.

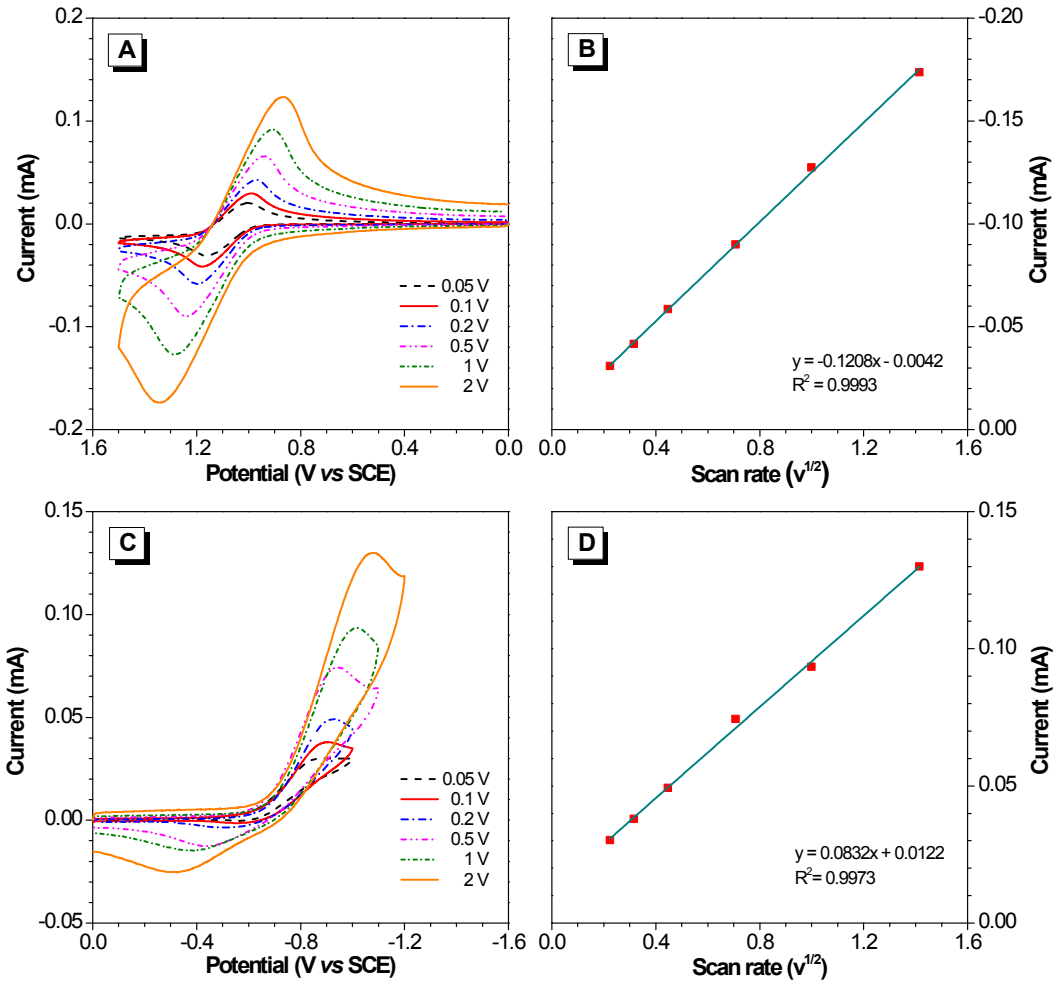

Fig. S11 Cyclic voltammograms of 1 mM **BTD-TPA** in DCM with 0.1 M $TBAPF_6$ at various scan rates; (A) oxidation voltammogram of **BTD-TPA**, (B) oxidation peak current *versus* $v^{1/2}$; (C) reduction voltammogram of **BTD-TPA**, (D) reduction peak current *versus* $v^{1/2}$.

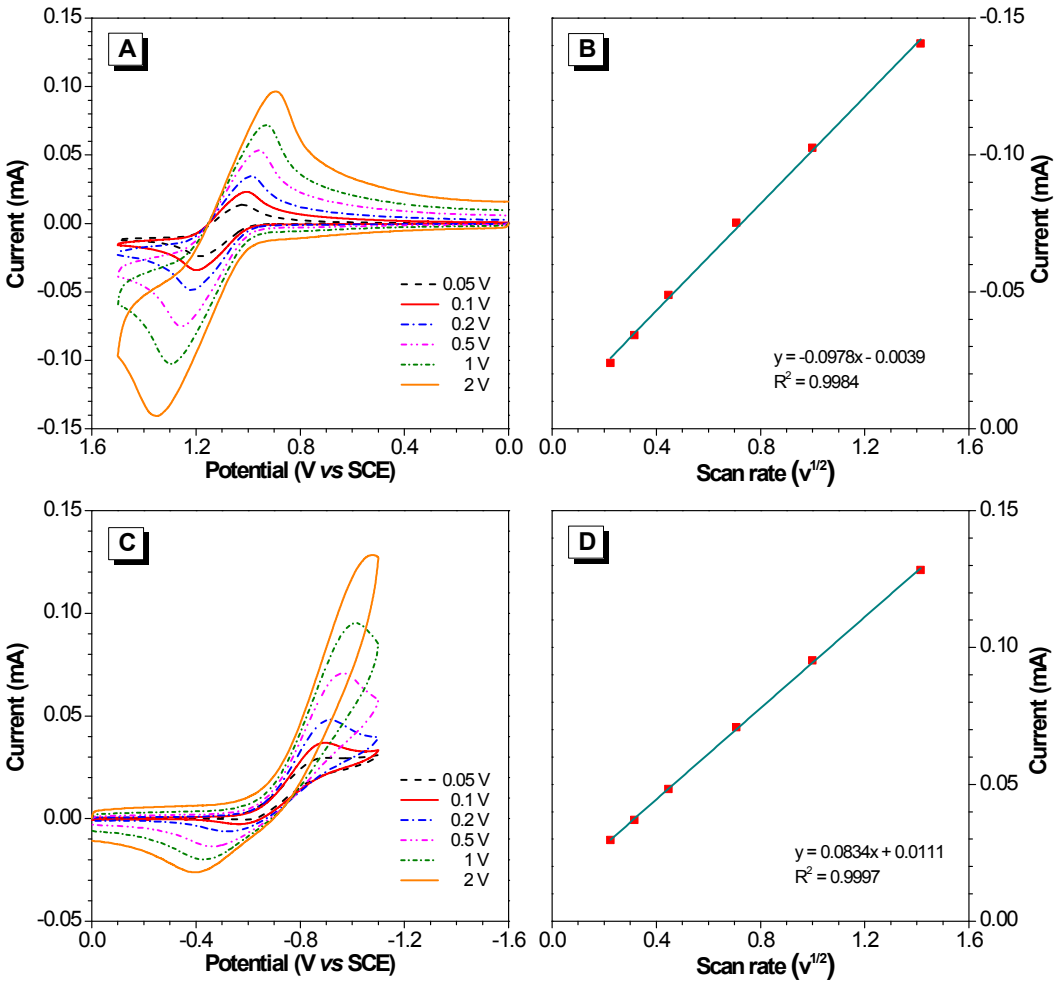

Fig. S12 Cyclic voltammograms of 1 mM **BTD-NPA** in DCM with 0.1 M $TBAPF_6$ at various scan rates; (A) oxidation voltammogram of **BTD-NPA**, (B) oxidation peak current *versus* $v^{1/2}$; (C) reduction voltammogram of **BTD-NPA**, (D) reduction peak current *versus* $v^{1/2}$.

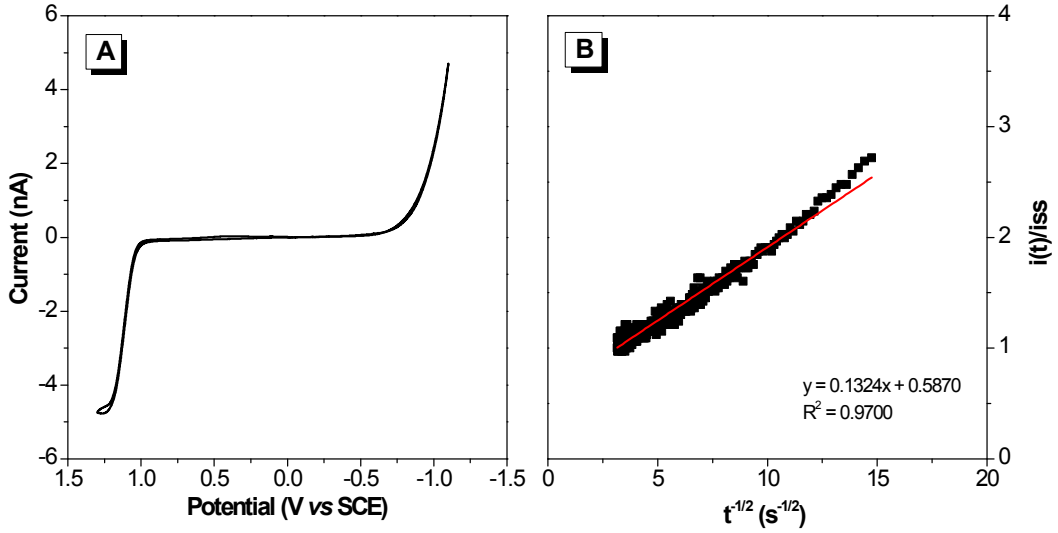

Fig. S13 (A) Cyclic voltammogram of 1 mM **BTD-TPA**. Scan rate is 0.05 V/s. (B) Plot of the experimental ratio $i_{(t)}/i_{ss}$ against the inverse square root of time for the oxidation of 1 mM **BTD-TPA** in 0.1 M $TBAPF_6$ with 12.5 μm radius Au UME in DCM.

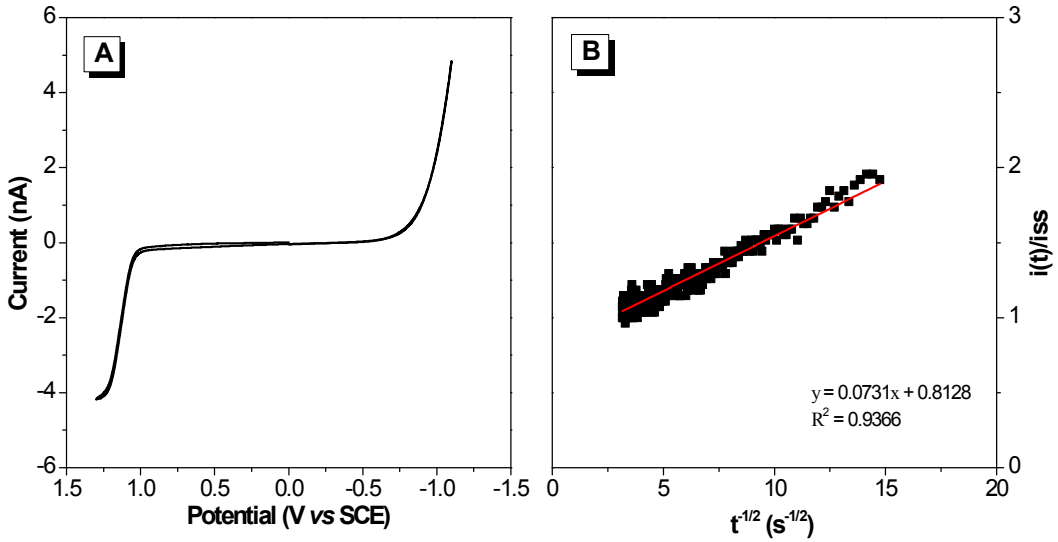

Fig. S14 (A) Cyclic voltammogram of 1 mM **BTD-NPA**. Scan rate is 0.05 V/s. (B) Plot of the experimental ratio $i_{(t)}/i_{ss}$ against the inverse square root of time for the oxidation of 1 mM **BTD-NPA** in 0.1 M $TBAPF_6$ with 12.5 μm diameter Au UME in DCM.

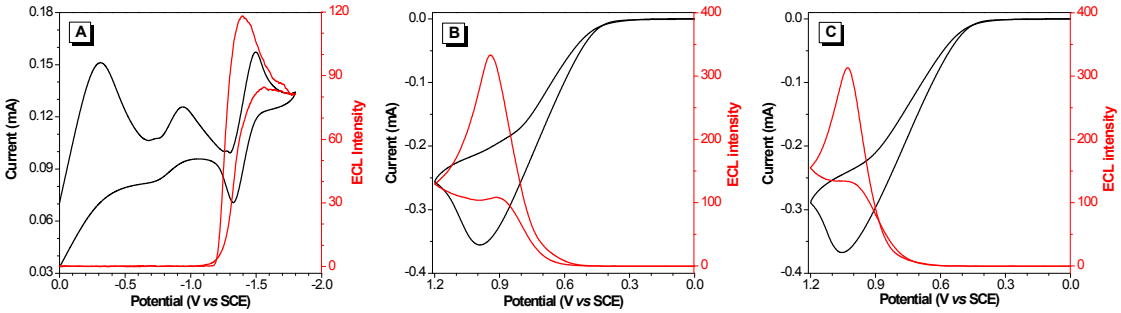

Fig. S15 CV (black line) and ECL (red line) profiles of 1 mM (A) **BTD-Ph**, (B) **BTD-TPA**, and (C) **BTD-NPA** in DCM solution.

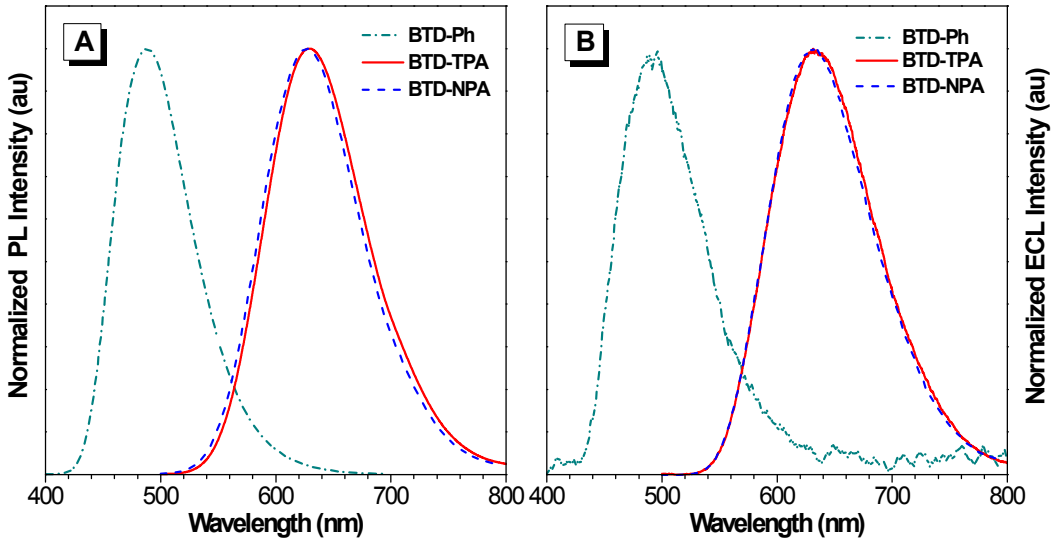

Fig. S16 (A) Normalized PL emission spectra of **BTD-Ph**, **BTD-TPA**, and **BTD-NPA** in DCM solution. Concentration: 10 μM; excitation wavelength: absorption maximum. (B) The ECL spectra of **BTD-Ph**, **BTD-TPA**, and **BTD-NPA** in DCM solution.

ECL spectra of **BTD-Ph**, **BTD-TPA**, and **BTD-NPA** resemble their corresponding PL spectra, which confirms that the ECL is indeed from the luminogens.[1]

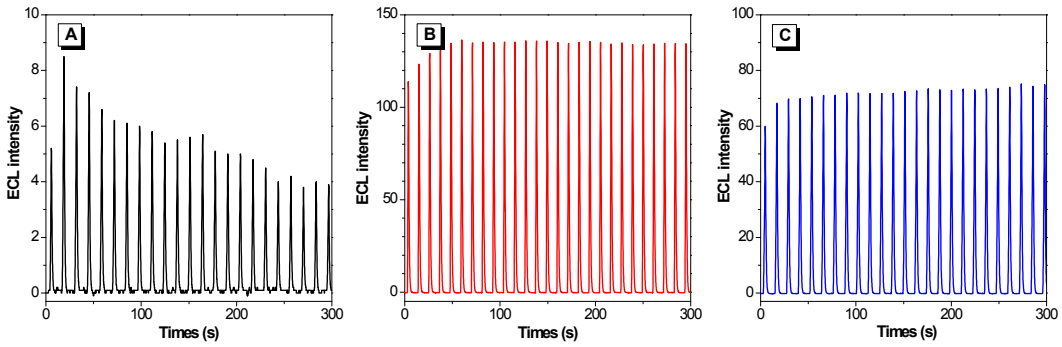

Fig. S17 ECL light transients for 1 mM (A) **BTD-Ph**, (B) **BTD-TPA**, and (C) **BTD-NPA** in DCM solution.

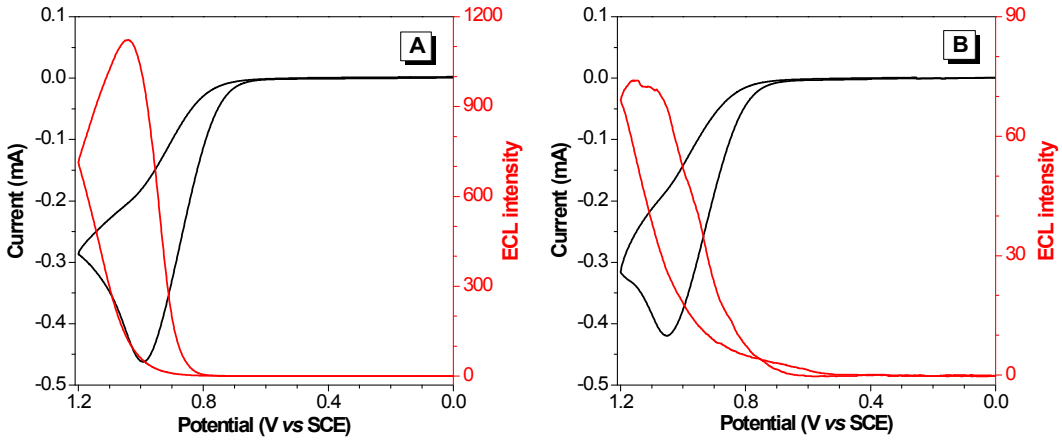

Fig. S18 CV (black line) and ECL (red line) profiles of the solid films of (A) **BTD-TPA** and (B) **BTD-NPA**.

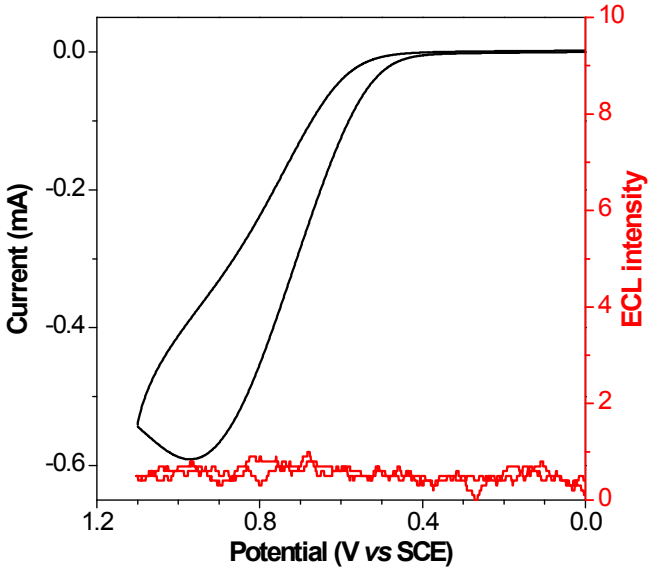

Fig. S19 CV (black line) and ECL (red line) profiles of bare GCE with 0.1 M $TBAPF_6$ as supporting electrolyte in the presence of 20 mM TPrA.

In the control experiment, the ECL signal of the bare GCE was not detected in the same experimental conditions.

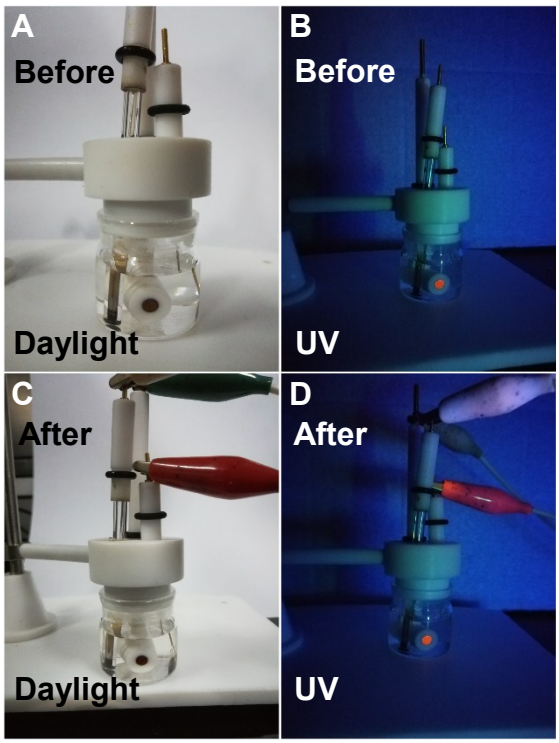

Fig. S20 Digital photos of experimental setup before the ECL experiment of **BTD-TPA** films (A) under daylight and (B) on UV illumination. Digital photos of experimental setup after the ECL experiment of **BTD-TPA** films (C) under daylight and (D) on UV illumination.

Digital photos of the experimental setup before and after the ECL experiment of the **BTD-TPA** films were taken (Fig. S20). The **BTD-TPA** film is insoluble in the supporting electrolyte before and after the ECL experiment. The result confirms that the bright ECL is generated from the solid film of **BTD-TPA**.

Determination of ECL efficiency

The ECL efficiencies were calculated using $Ru(bpy)_3^{2+}$ in acetonitrile as reference (Φ_{ECL} = 5.0%) by integration of both ECL intensity and current value versus time for each compound, as described in Equation (S1)[2]

$$\Phi_x = 100\% \times \left[\frac{\int_a^b ECLdt}{\int_a^b Currentdt}\right]_x / \left[\frac{\int_a^b ECLdt}{\int_a^b Currentdt}\right]_{st} \quad \text{(S1)}$$

where *x* stands for **BTD-TPA** and **BTD-NPA**, and *st* represents $Ru(bpy)_3^{2+}$.

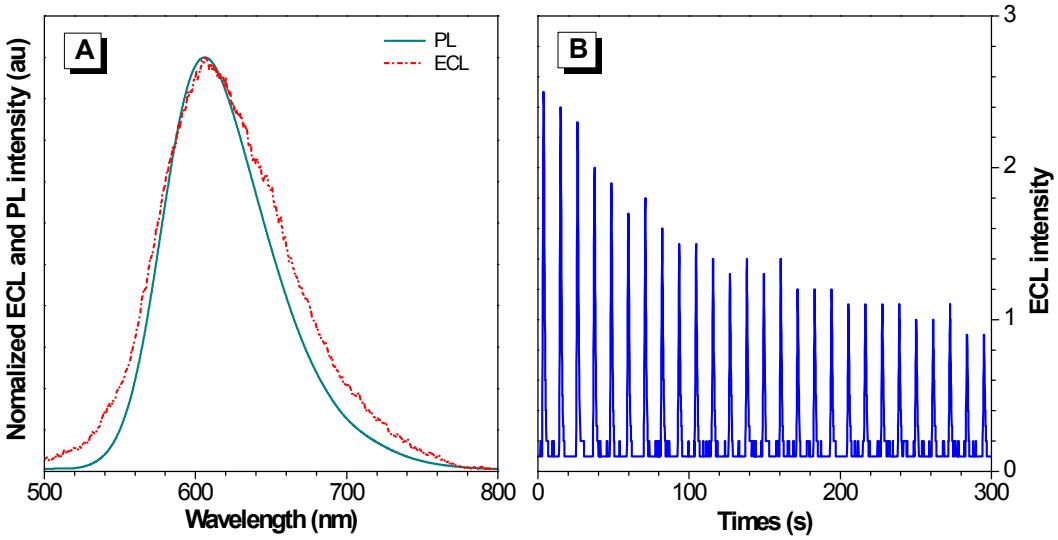

Fig. S21 (A) Normalized ECL and PL emission spectra of the **BTD-NPA** film. Excitation wavelength: 460 nm. (B) The ECL stability of the **BTD-NPA** film on GCE.

The proposed mechanism of ECL of BTD-TPA films

BTD-TPA $- e^- \rightarrow$ BTD-TPA$^{\cdot+}$ (oxidation at electrode) (S2)

TprA $- e^- \rightarrow$ TprA$^{\cdot+}$ (oxidation at electrode) (S3)

TprA$^{\cdot+} \rightarrow$ TprA$^{\cdot+} + H^+$ (reducing species formation) (S4)

BTD-TPA$^{\cdot+} +$ TprA$^{\cdot} \rightarrow$ BTD-TPA* (excited state formation) (S5)

BTD-TPA* $\rightarrow$ BTD-TPA $+ h\nu$ (light emission) (S6)

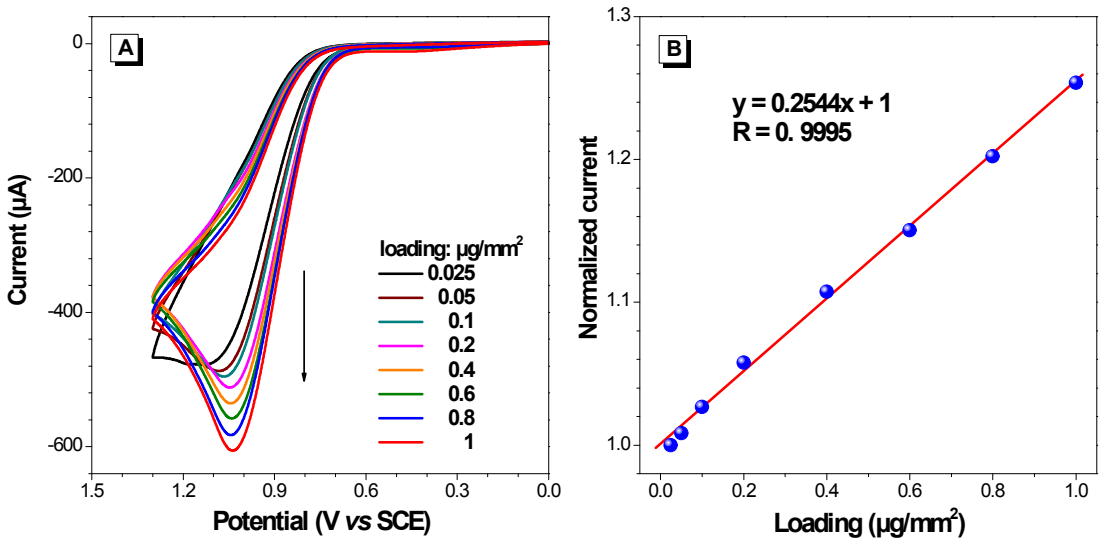

Fig. S22 (A) CVs of **BTD-TPA** films at various loadings in the presence of 0.1 M $TBAPF_6$ as supporting electrolyte and 20 mM TPrA. (B) Plot of relative current *versus* **BTD-TPA** loading.

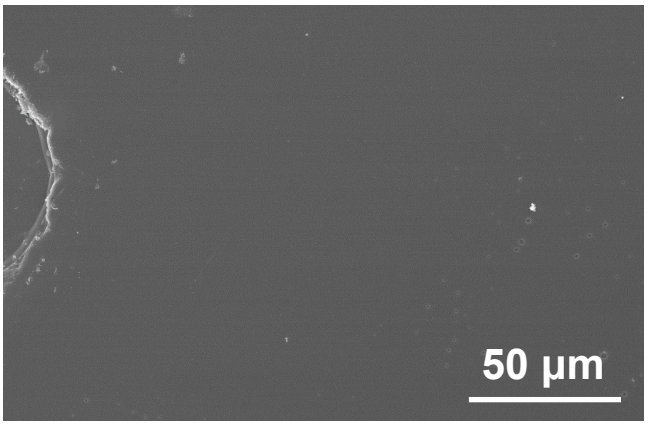

Fig. S23 SEM image of **BTD-TPA** films on GCE.

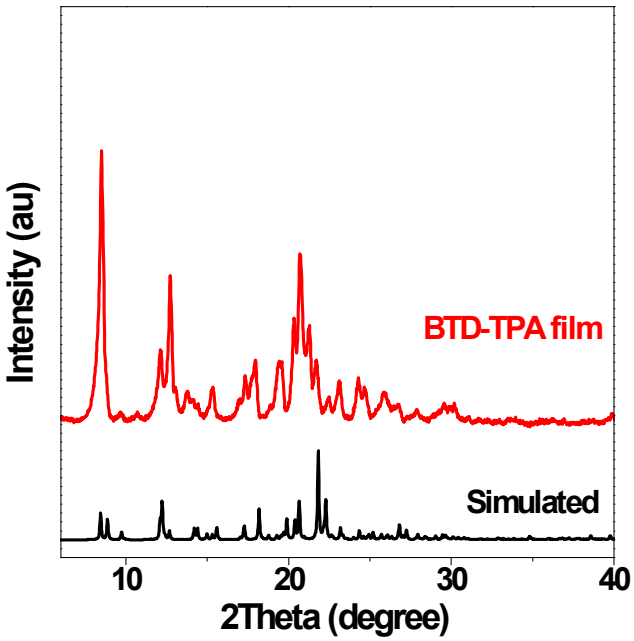

Fig. S24 The XRD pattern of **BTD-TPA** films (black line: simulated from the single crystal).

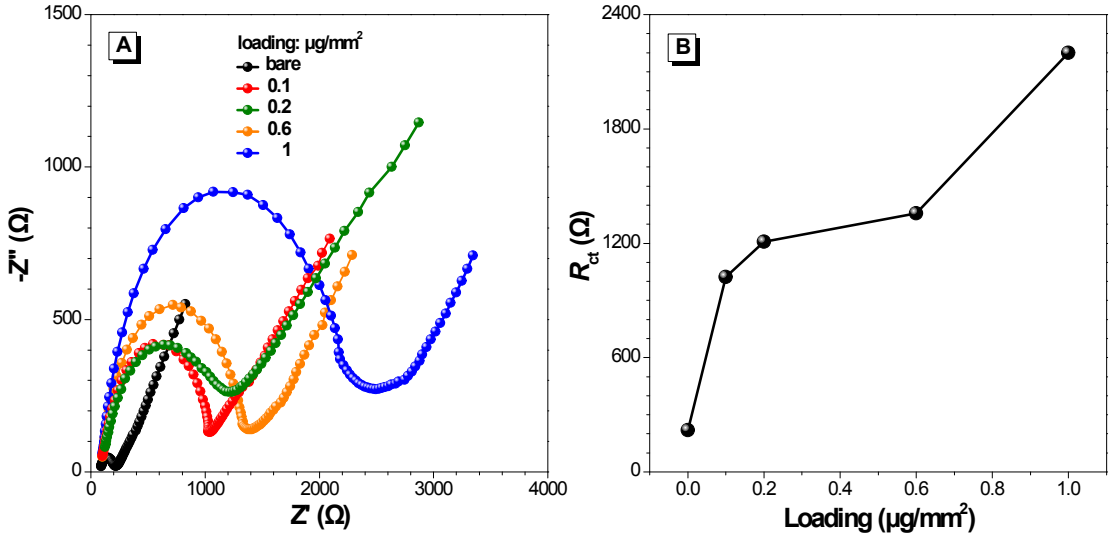

Fig. S25 (A) EIS profiles of **BTD-TPA** films on GCE at different loadings in 5mM $K_3[Fe(CN)_6]/K_4[Fe(CN)_6]$ (molar ratio = 1:1) solution containing 0.1 M KCl. (B) Plots of the R_{ct} value *versus* **BTD-TPA** loading.

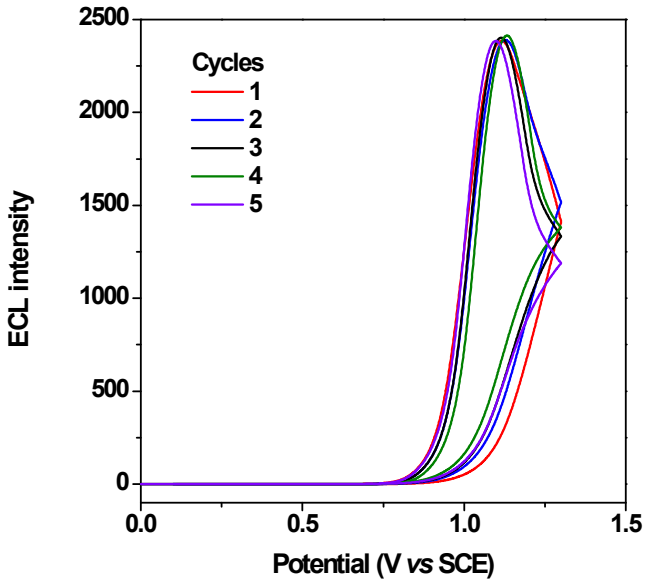

Fig. S26 ECL intensity-potential profiles of the **BTD-TPA** films in the absence of DA during consecutive scanning.

Calculation of the detection limits of DA, AA, and UA

$DL = 3\sigma / K_{SV}$ (S7)

DL = 3×(0.0031/0.5456) = 17.0 nM (DA)

DL = 3×(0.0031/0.0009) = 10.3 μM (AA)

DL = 3×(0.0031/0.5701) = 18.6 μM (UA)

where DL is detection limit of a quencher, σ represents the standard derivation and K_{SV} denotes the slope of the Stern-Volmer plot. The detection limits of AA and UA are calculated to be 1.03×10^4 and 1.86×10^4 nM, respectively.

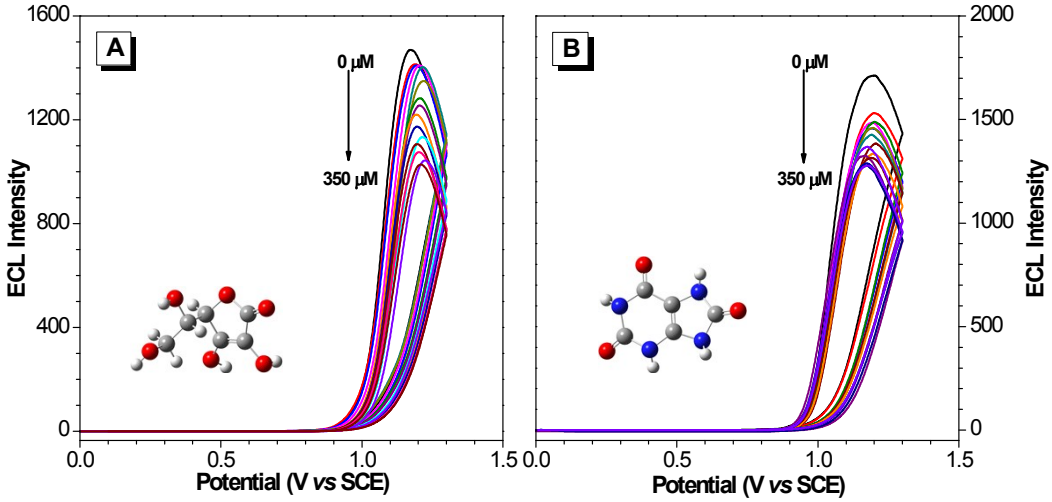

Fig. S27 ECL intensity-potential profiles of the **BTD-TPA** film with different concentration of (A) AA and (B) UA: 0 to 350 μM (top to bottom).

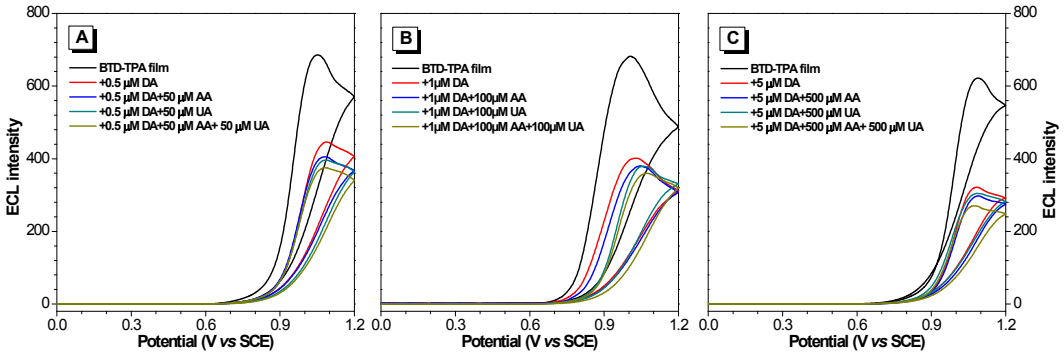

Fig. S28 ECL intensity-potential profiles of the **BTD-TPA** film with different concentration of (A) 0.5 μM DA in the presence of 50 μM AA, UA and mixtures of AA and UA; (B) 1 μM DA in the presence of 100 μM AA, UA and mixtures of AA and UA; and (C) 5 μM DA in the presence of 500 μM AA, UA and mixtures of AA and UA.

To demonstrate high selectivity of the ECL detection method, we conducted interference experiments (Fig. S28). The ECL intensity of **BTD-TPA** films is dramatically decreased after addition of 1 μM DA with 62.5% of its initial ECL intensity. It is noteworthy that after addition of the mixtures containing DA (1 μM) and plenty amount of interferential analytes (100 μM), the ECL intensity maintains slight variations with the values of 59.1% for DA+AA, 58.8% for DA+UA, and 55.6% for DA+AA+UA (Fig. S28B). Similar results were obtained after addition of different concentrations of DA (0.5 and 5 μM) and excessive amount of interferential analytes (Fig. S28A and S28C). The results indicate high selectivity of **BTD-TPA** ECL films toward DA.

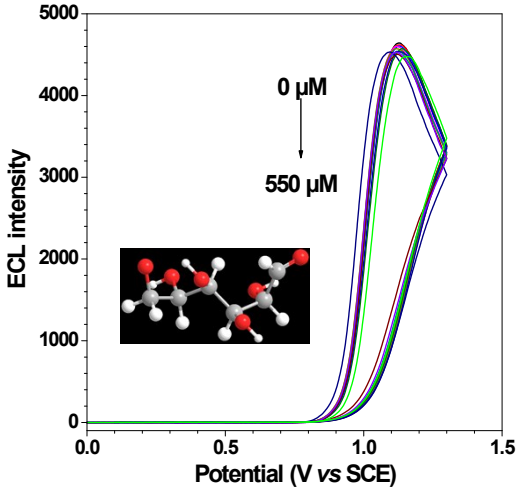

Fig. S29 The plots of ECL intensity against potential for **BTD-TPA** films with various concentrations of glucose.

BTD-TPA films were employed to the detection of glucose. As shown in Fig. S29, the ECL intensity of **BTD-TPA** films is almost unchanged with the addition of glucose.

Table S2. Comparison of this work with other biosensors for detection of DA.

Electrodes	Method	Quenching constant	Linear range	Detection limit	Reference
		[$\times 10^5$ M^{-1}]	[μM]	[nM]	
DPA-CM NPs/GCE[a]	ECL	2.9	0.05 to 50	400	3
RGO/MWCNTs/AuNPs/GCE[b]	ECL	-	0.2 to 70	67	4
Ag_2Se quantum dots/GCE	ECL	2.0	0.5 to 19	100	5
Cu@CdInS nanoclusters/GCE	ECL	-	0.5 to 100	355	6
Poly(chromotrope 2B)/GCE	DPV[g]	-	0.4 to 1	40	7
Au/rGO/GCE	DPV	-	6.8 to 41	1400	8
Cu2-modified Au electrode[c]	DPV	-	0.2 to 30	80	9
RGO-ZnO/GCE	DPV	-	3 to 330	1080	10
Molecular imprinting polymer/GCE	DPV	-	0.05 to 10	33	11
PA6/PAH_MWCNTs/ITO[d]	DPV	-	1 to 70	150	12
Graphene-diamond hybrid electrode	DPV	-	5 to 2000	200	13
GNB	DPV	-	2 to 202	580	14
Au@CDs-CS/GCE	DPV and CV	-	0.01 to 100	1	15
PEDOT modified LSGE[e]	DPV and CV	-	1 to 150	330	16
Electrochemically rGO/GCE	CV	-	0.5 to 60	500	17
GO-BAMB-$Co(OH)_2$/GCE[f]	CV	-	3 to 100	400	18
BTD-TPA film/GCE	**ECL**	**5.5 and 0.66**	**0.05 to 350**	**17**	**This work**

[a]DPA-CM NPs: 6-[4-(N,N-diphenylamino)phenyl]-3-ethoxycarbonyl coumarin nanoparticles. [b]RGO/MWCNTs: reduced graphene oxide/multiwalled carbon nanotubes. [c]Cu2: $[Cu_2Cl_2(mtboc)_2(C_{12}H_8N_2)_2]$ [mtboc: 2-(methylthio)benzo[*d*]oxazole-5-carboxylic acid]. [d]PA6/PAH: polyamide 6/poly(allylamine hydrochloride) (PA6/PAH) nanofibers. [e]PEDOT modified LSGE: poly(3,4-ethylenedioxythiophene) modified laser scribed graphene electrode. [f]BAMB: 1,4-bis(aminomethyl)benzene. [g]DPV: differential pulse voltammetry measurements.

References

1 J. Suk, P. Natarajan, J. N. Moorthy and A. J. Bard, *J. Am. Chem. Soc.*, 2012, **134**, 3451-3460.

2 K. N. Swanick, S. Ladouceur, E. Zysman Colman and Z. Ding, *Chem. Commun.*, 2012, **48**, 3179-3181.

3 H. Liu, L. Wang, H. Gao, H. Qi, Q. Gao and C. Zhang, *ACS Appl. Mater. Interfaces*, 2017, **9**, 44324-44331.

4 D. Yuan, S. Chen, R. Yuan, J. Zhang and X. Liu, *Sensor Actuat. B-Chem.*, 2014, **191**, 415-420.

5 R. Cui, Y. P. Gu, L. Bao, J. Y. Zhao, B. P. Qi, Z. L. Zhang, Z. X. Xie and D. W. Pang, *Anal. Chem.*, 2012, **84**, 8932-8935.

6 F. Wang, J. Lin, H. Wang, S. Yu, X. Cui, A. Ali, T. Wu and Y. Liu, *Nanoscale*, 2018, **10**, 15932-15937.

7 X. B. Li, M. M. Rahman, G. R. Xu and J. J. Lee, *Electrochim. Acta*, 2015, **173**, 440-447.

8 C. Wang, J. Du, H. Wang, C. e. Zou, F. Jiang, P. Yang and Y. Du, *Sensor Actuat. B-Chem.*, 2014, **204**, 302-309.

9 G. Jiang, X. Gu, G. Jiang, T. Chen, W. Zhan and S. Tian, *Sensor Actuat. B-Chem.*, 2015, **209**, 122-130.

10 X. Zhang, Y. C. Zhang and L. X. Ma, *Sensor Actuat. B-Chem.*, 2016, **227**, 488-496.

11 M. Zhong, Y. Teng, S. Pang, L. Yan and X. Kan, *Biosens. Bioelectron.*, 2015, **64**, 212-218.

12 L. A. Mercante, A. Pavinatto, L. E. O. Iwaki, V. P. Scagion, V. Zucolotto, O. N. Oliveira, L. H. C. Mattoso and D. S. Correa, *ACS Appl. Mater. Interfaces*, 2015, **7**, 4784-4790.

13 Q. Yuan, Y. Liu, C. Ye, H. Sun, D. Dai, Q. Wei, G. Lai, T. Wu, A. Yu, L. Fu, K. W. A. Chee and C. T. Lin, *Biosens. Bioelectron.*, 2018, **111**, 117-123.

14 P. K. Kannan, S. A. Moshkalev and C. S. Rout, *Nanotechnol.*, 2016, **27**, 075504.

15 Q. Huang, H. Zhang, S. Hu, F. Li, W. Weng, J. Chen, Q. Wang, Y. He, W. Zhang and X. Bao, *Biosens. Bioelectron.*, 2014, **52**, 277-280.

16 G. Xu, Z. A. Jarjes, V. Desprez, P. A. Kilmartin and J. Travas Sejdic, *Biosens. Bioelectron.*, 2018, **107**, 184-191.

17 L. Yang, D. Liu, J. Huang and T. You, *Sensor Actuat. B-Chem.*, 2014, **193**, 166-172.

18 A. Ejaz, Y. Joo and S. Jeon, *Sensor Actuat. B-Chem.*, 2017, **240**, 297-307.